


Article

Taxifolin Adsorption on Nitrogenated Graphenes: Theoretical Insights

Igor Petrushenko 

Irkutsk National Research Technical University, 83 Lermontov St., 664074 Irkutsk, Russia;
igor.petrushenko@istu.edu

Abstract: Solid-state drug delivery systems for the drug substances transport are of great importance nowadays. In the present work, the non-covalent interactions between taxifolin (**Tax**) and graphene as well as nitrogenated (N-doped) graphenes were systematically studied by using a wide set of theoretical techniques. Symmetry-adapted perturbation theory (SAPT0) calculations confirmed more favorable adsorption of **Tax** on N-doped graphenes compared to pristine graphene. It was established that dispersion interactions play the main role in the attractive interactions (>60%), whereas electrostatic and induction forces contribute only moderately to the attraction (~25% and 7–8%, respectively). Independent gradient model (IGM) analysis visually demonstrated the existence of dispersion interactions and hydrogen bonding in the studied **Tax** complexes. Ab initio molecular dynamics calculations indicated stability of these complexes at different temperatures. Our results show that N-doped graphenes with the enhanced interaction energy (E_{int}) toward **Tax** are promising candidates for the technical realization of the targeted drug delivery systems.

Keywords: graphene; taxifolin; nitrogenation; interaction energy; DFT; SAPT0



Citation: Petrushenko, I. Taxifolin Adsorption on Nitrogenated Graphenes: Theoretical Insights. *Solids* **2024**, *5*, 341–354. <https://doi.org/10.3390/solids5030023>

Academic Editors: Kejiang Li, Guangyue Li, Qifan Zhong and Stefano Agnoli

Received: 27 February 2024

Revised: 27 May 2024

Accepted: 24 June 2024

Published: 1 July 2024



Copyright: © 2024 by the author. Licensee MDPI, Basel, Switzerland. This article is an open access article distributed under the terms and conditions of the Creative Commons Attribution (CC BY) license (<https://creativecommons.org/licenses/by/4.0/>).

1. Introduction

In the last decade, scientific efforts have focused on the development of novel drug delivery systems (DDSs) for the transport of drug substances with marginal negative effects on the human organism. The need for highly efficient, flexible and controlled loading/release systems is driven by significant advances in patient compliance, clinical efficacy, and extended drug shelf life through controlled drug release. For these reasons, new DDSs have the potential to become one of the fastest growing segments of the pharmaceutical industry. It is believed that such systems can help one to overcome the limitation of bioavailability of different drugs and increase their efficiency for the introduction of novel therapies and theranostics. Current DDSs are based on nanostructural materials, and have been shown to offer substantial advantages, such as solubility, bioavailability, pharmacological activity, targeted delivery, and degradation [1–3].

Various available nanocarriers (e.g., carbon nanomaterials, metal and polymeric nanoparticles) have been widely used for drug delivery in cancer treatment [4–6]. Among them we may select graphene [7], graphene oxide [8], N-doped graphene [9], carbon nanotubes [10], and carbon nano-onions [11] as systems for drug delivery and release. Graphene-related materials have attracted much attention due to their biocompatibility [12] and valuable properties such as high specific surface area, ability for non-covalent π - π stacking, favorable interactions with various biomolecules, and high mechanical strength [8,13].

Taxifolin (**Tax**, dihydroquercetin) is a natural compound that belongs to the class of flavonoids. Much attention has been paid to **Tax** owing to its important pharmacological properties [14]. It is a powerful antioxidant with a pronounced effect in the prevention of several forms of cancer. Recently, it has shown promising suppressive activity against inflammation, malignancies, microbial infections, and cardiovascular and liver diseases. In present time, the protective role of **Tax** as a COVID-19 recovery is being evaluated (see, e.g., the recent review and the references therein [14]).

Different works reported a successful **Tax** release performance by zinc oxide nanoparticles [15], collagen-acrylic hydrogels [16], zein-caseinate nanoparticles [17], and cyclodextrine [18]. However, the papers dealing with interactions between **Tax** molecules and graphene derivatives are rather scarce. The bright examples are the work of Zhao et al. on quercetin, luteolin, and kaempferol adsorption on graphene oxide (GO) [19] and the paper of Tiwari et al. on quercetin adsorption on GO [20], and the report of Garcia et al. on a family of selected flavonoids and pristine graphene [21].

This work investigates adsorption properties of nanostructured platforms consisting of nitrogenated (N-doped) graphenes as nanocarriers loaded with the **Tax** molecule. N-doped carbon materials are among the most efficient metal-free catalysts [22]. It was found earlier that N-doping of graphene can slightly increase the activity of the oxygen reduction reaction, but N-doping at the graphene interface does not contribute significantly to the activity enhancement [23]. Also, N-doped graphenes have been studied for electrochemical sensing applications owing to their ability to enhance conductivity [24]. In addition to various catalytic applications, other applications can be found in medicine as N-doped graphene materials exhibit reduced cytotoxicity and antioxidant effects in a nitrogen content-dependent manner [25]. Moreover, N-doped graphene materials show less toxicity compared to GO [26].

More specifically, our aim is to perform a thorough comparative analysis of adsorption properties of graphene (**G**) and N-graphenes (pyrrolic (**Npyrr-G**), pyridinic (**Npyrid-G**) and quaternary graphene (**2N-G**)) toward **Tax** by using density functional theory (DFT), symmetry adapted perturbation theory (SAPT0) [27,28], the quantum theory of atoms-in-molecules (QTAIM) [29], and the independent gradient model (IGM) method [30,31]. Ab initio molecular dynamics (AIMD) simulations reveal the behavior of all complexes at room and liquid nitrogen temperatures. We suggest that the present theoretical study reveals the features of **Tax**/adsorbent interactions, indicating a promising future for nanoscale DDSs.

2. Computational Details

Geometries of the studied **Tax** complexes were optimized at the BLYP-D3/def2-SVP [32–34] level using the Orca 5.0.3 package [35]. Grimme's dispersion correction (D3) was employed to properly treat van der Waals interactions [36]. The BLYP-D3 functional has been shown to provide reliable results on non-covalent complexes [37,38]. For each of these complexes, the total interaction energy (E_{int}) was calculated using the 0th-order symmetry-adapted perturbation theory (SAPT0) method [27] with the jun-cc-pVDZ basis set [39,40], which allows decomposing E_{int} to the exchange (E_{ex}), electrostatic (E_{el}), dispersion (E_{disp}), and induction (E_{ind}) components. It was established that such a combination of methods accurately predicts adsorption energies. SAPT0 calculations were carried out using the Psi4 code (v.1.4) [41]. It should be noticed that the more negative E_{int} value for a given complex denotes the stronger adsorption. The simplest SAPT0 method is defined in the following equation [28]:

$$E_{SAPT0} = E_{elst}^{(10)} + E_{exch}^{(10)} + E_{ind,resp}^{(20)} + E_{exch-ind,resp}^{(20)} + E_{disp}^{(20)} + E_{exch-disp}^{(20)} + \delta_{HF}^{(2)}$$

In this notation, $E^{(vw)}$ defines the order in V and in $W_A + W_B$ in the Hamiltonian (H):

$$H = F_A + W_A + F_B + W_B + V,$$

where the H is written as a sum of the usual monomer Fock operators (F), the fluctuation potential of each monomer (W), and the interaction potential (V); the subscript (resp) indicates that orbital relaxation effects are included.

The $\delta_{HF}^{(2)}$ term takes into account the higher-order induction effects, and it is included in the definition of SAPT terms.

Normally, the adsorption energy terms are calculated as following:

$$E_{int} = E_{el} + E_{ex} + E_{ind} + E_{disp},$$

where $E_{el} = E_{elst}^{(10)}$, $E_{ex} = E_{exch}^{(10)}$

$$E_{ind} = E_{ind,resp}^{(20)} + E_{exch-ind,resp}^{(20)} + \delta_{HF}^{(2)} E_{disp} = E_{disp}^{(20)} + E_{exch-disp}^{(20)}$$

We should briefly describe the components of the E_{int} energy term [42]. The electrostatic effect (E_{el}) describes the classical interactions between the static charge distributions of the interacting species. It may be either attractive (−) or repulsive (+). Induction effects (E_{ind}) arise from the distortion of a molecule in response to the electric field of all neighbor molecules, and they are always attractive (−). Dispersion interactions (E_{disp}) arise owing to instantaneous fluctuations of electron distributions of the molecules, and they are also attractive (−). The Pauli or exchange (E_{ex}) repulsion can be described from a classical point of view. The atomic approach results in a decrease in electron density in the internuclear region. As a result, the decreased screening of nuclear charges occurs, which leads to the increased nuclear-nuclear repulsion (+).

The studied model of graphene (**G**) consists of 48 carbon atoms. Three major cases of N-doped graphenes, namely pyrrolic (**Npyrr-G**), pyridinic (**Npyrid-G**) and quaternary graphene (**2N-G**) were also used as adsorbents. These models were chosen according to the experimental work on N-graphenes [43]. Their stability has been reported elsewhere [44]. The peripheral rims of all adsorbent models were saturated with hydrogen atoms to avoid dangling. The nanosheets of similar sizes have been recently employed as models for different adsorption studies [44,45].

The procedure for energy calculations was as follows. Firstly, to obtain the minimum energy structure, the **Tax** molecule was placed above the adsorbent sheet at a height corresponding the physisorbed state (~3.0 Å) and allowed to relax freely. The mutual initial configurations were randomized (see Figures S1–S4). The minimum energy configuration was used as the input configuration for SAPT0 calculations.

The initial structures for ab initio molecular dynamics (AIMD) simulations were also relaxed using the BLYP/def2-SVP method. All AIMD simulations used a time step of 1 fs, an NVT ensemble using a Nose–Hoover thermostat, and a velocity Verlet algorithm for integrating the equation of motion. The time period of 1000 fs has been used for the full AIMD computation cycle. These calculations were also done using the Orca 5.0.3 program suite.

The Multiwfn 3.8.0 program [46] has been used to obtain the independent gradient model (IGM) [30,31] isosurfaces and as well as obtaining the QTAIM parameters. VMD (v.1.9.3) [47] and Chemcraft [48] programs have been used for visualization aims. The detailed description of the IGM analysis has been given in the Supplementary Materials.

3. Results and Discussions

The models used for **Tax**, graphene and N-graphenes are demonstrated in Figures 1 and 2. Table 1 shows the calculated interaction energy (E_{int}) and its constituents for **Tax** adsorption obtained at the SAPT0/jun-cc-pVDZ level of theory. To figure out the possible influence of the size of the adsorbent on the E_{int} values, we consider larger graphene sheets compared to the studied model. Generally, the widely used graphene model (circumcoronene) consists of 54 C atoms [49]. Also, we involve into consideration the graphene model consisting of 80 C atoms (Figure S5). The total E_{int} values are calculated to be −31.05 kcal/mol for the former and −33.72 kcal/mol for the latter. These values are in a good accordance with that for **Tax** adsorption on **G** presented herein (−30.04 kcal/mol). We, hence, proceed with the initial model.

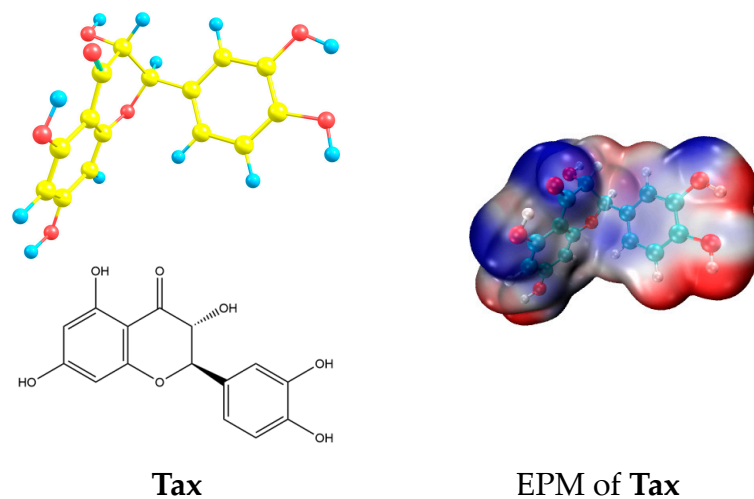


Figure 1. Molecular structure and EPM of Tax (isovalue = 0.001). Color code: blue—electron density gain, red—electron density depletion. Atomic color code: hydrogen—light-blue, oxygen—red, and carbon—yellow.

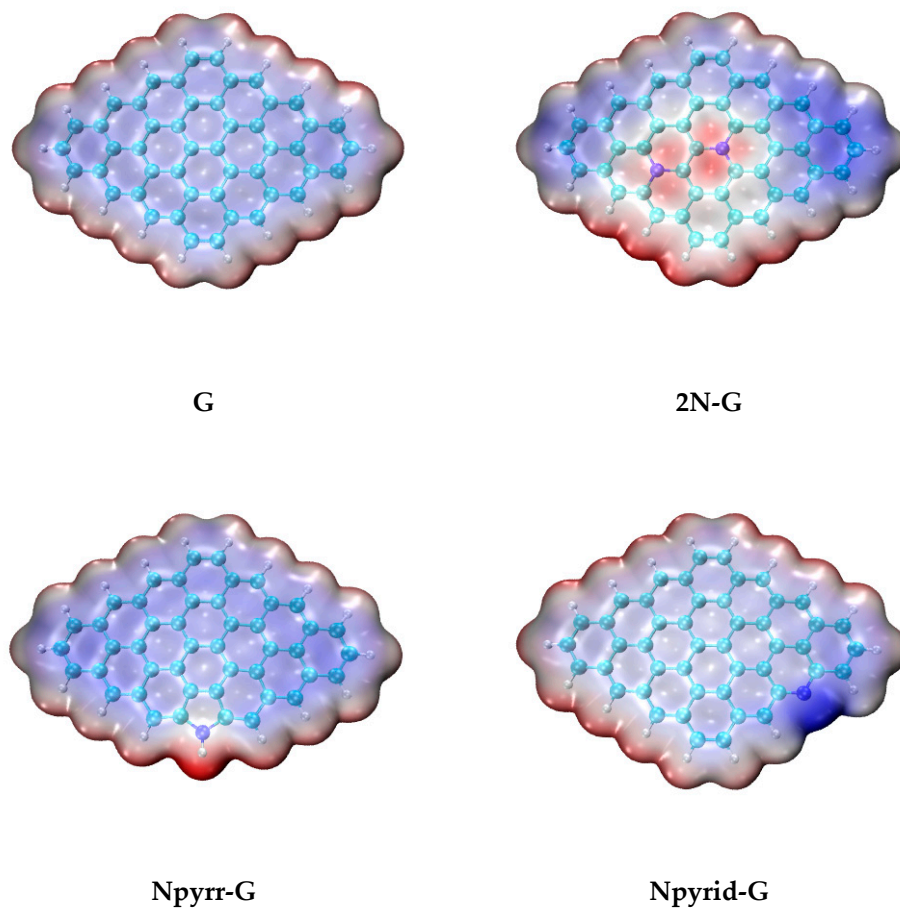


Figure 2. Four adsorbents studied in this work. Color code: deep blue—electron accumulation, deep red—electron depletion (isovalue = 0.001). Atomic color code: hydrogen—white, carbon—diamond-green, and nitrogen—blue.

Table 1. E_{int} and its constituents (kcal/mol) for interactions between **Tax** and the studied adsorbents. The values in parentheses denote the percentage contribution to attractive energy.

Adsorbent	E_{int}	E_{el}	E_{ex}	E_{ind}	E_{disp}
G	−30.04	−17.02 (25.0)	38.11	−4.80 (7.0)	−46.32 (68.0)
Npyrid-G	−37.16	−22.01 (23.8)	55.33	−7.46 (8.1)	−63.01 (68.1)
Npyrr-G	−32.63	−17.64 (23.3)	43.06	−6.21 (8.2)	−51.84 (68.5)
2N-G	−43.42	−28.34 (26.9)	62.12	−9.18 (8.7)	−68.02 (64.4)

First, we analyze the E_{int} energy term and its components for **Tax** adsorption. The magnitude of E_{int} for pristine graphene is the smallest one. At the same time, the gradual increase in E_{int} from **Npyrr-G** (−32.63 kcal/mol) to **Npyrid-G** (−37.16 kcal/mol) and further to **2N-G** (−43.42 kcal/mol) is observed. It is of note, that the last case represents a much larger E_{int} value compared to E_{int} for graphene (~40%). To study these differences in detail, we now consider the electrostatic, inductive and dispersion contributions to the total attraction energy for all adsorbents. First, the marked increase in E_{el} can be observed for N-graphenes, except for the case of **Npyrr-G** (Table 1). The most significant E_{el} value of −28.34 kcal/mol is in the case of **Tax/2N-G** interactions. Besides this, only the **2N-G** structure shows an increase in the relative contribution of E_{el} to E_{int} (26.9%).

We use electrostatic potential maps (EPMs) to further study electrostatic contributions in non-covalent interactions between the four adsorbents and **Tax** (Figures 1 and 2). Blue areas characterize the abundance of electrons (negative charge), whereas red areas exhibit electron depletion (positive charge). For **Tax**, the negatively charged regions can be observed at O atoms, whereas positively charged regions are located at H atoms of OH groups (Figure 1). Figure 2 shows that, in contrast to the pristine G structure, all N-graphenes show non-uniform EPMS. **2N-G** is characterized by the electron-depleted central area and electron-rich peripheral regions. At the same time, pyrrolic and pyridinic N atoms introduce marked changes at the edge of the **Npyrr-G** and **Npyrid-G** models, respectively. At a qualitative level, we may assume that the substituted benzene rings of **Tax** would interact with graphenes via π - π stacking. The OH-groups of **Tax** may preferably interact with the π -system of G and N-graphenes through H-bonding. As a whole, non-uniform EPMS of N-graphenes and especially of **2N-G** will enhance intermolecular electrostatic interactions. These facts support our results obtained from SAPT0 calculations, which exhibit notable contributions of such interactions to the total attraction. The Mulliken charge transfer (CT) is calculated to be 0.031, 0.050, 0.064, and 0.025 e-towards **G**, **2N-G**, **Npyrid-G**, and **Npyrr-G**, respectively. The larger CT values are attributed to the cases of larger interactions between **Tax** and N-graphenes (**2N-G** and **Npyrid-G**).

The independent gradient model (IGM) method allows the types of non-covalent interactions between interacting species to be obtained through a simple analysis of colored 3D isosurfaces. The isosurfaces obtained in the framework of IGM indicate the existence of two types of interactions between **Tax** and four adsorbents studied herein.

According to the IGM method, we can easily conclude that the stronger interactions (blue-colored areas of isosurfaces) are hydrogen bonding (H-bonding), and the weaker binding (green-colored areas of isosurfaces) is due to van der Waals interactions (Figure 3). The vast areas of green-colored isosurfaces are consistent with the results of SAPT0 calculations. This approves the importance of dispersion interactions for the favorable accommodation of **Tax** molecules on the surfaces of pristine graphene and N-graphenes. For the further examination of intermolecular interactions, we involve the Bader's QTAIM analysis [29].

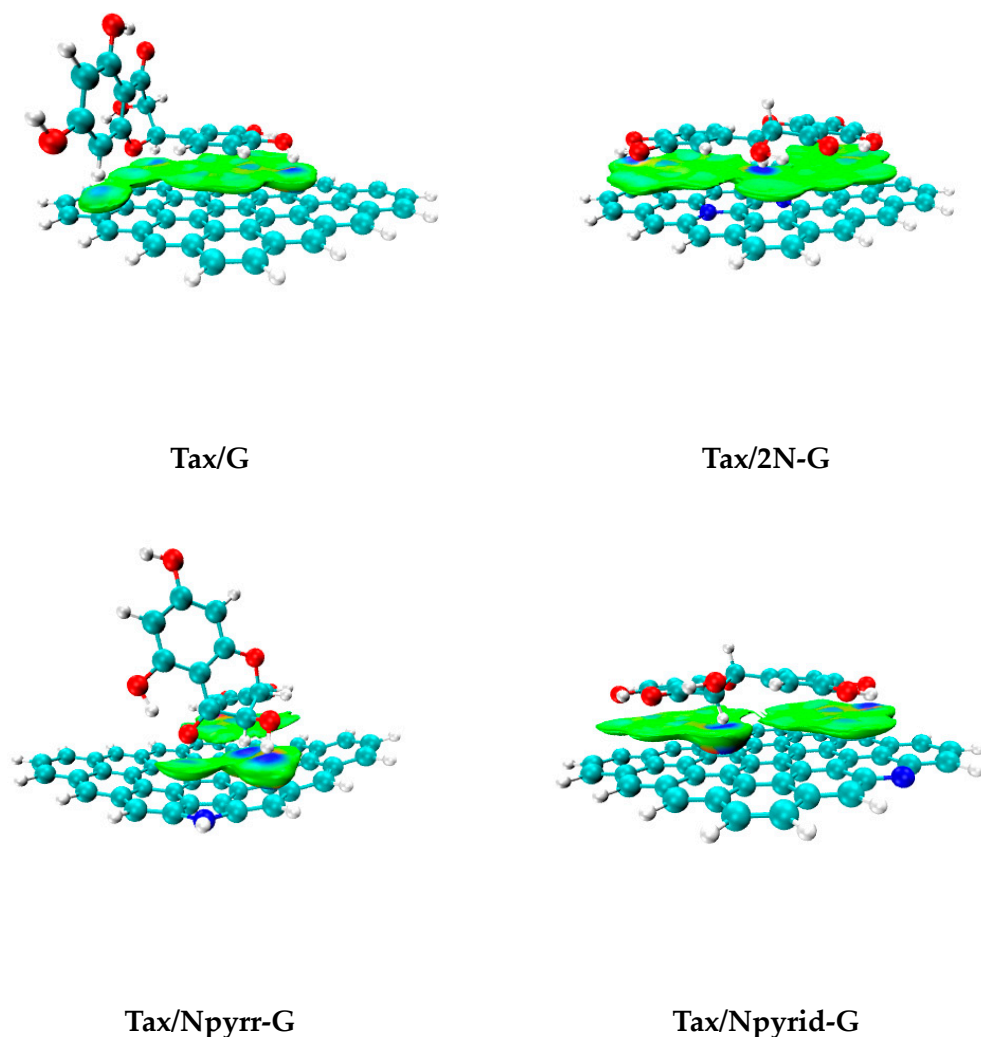


Figure 3. The IGM isosurfaces (isovalue = 0.005) for **Tax** adsorption on all studied adsorbents. Green isosurfaces denote weak van der Waals interactions, whereas blue denote strong attractive interactions. Atomic color code is the same as in Figure 2.

According to the Koch and Popelier's QTAIM criteria for the existence of H-bonding, the following conditions should be fulfilled: first, the bond critical point (BCP) (3,−1) for the proton/acceptor contact exists; second, the electron density $\rho(\mathbf{r})$ value for BCP (3,−1) should be in the range of 0.002 to 0.034 a.u.; and third, the corresponding Laplacian, $\nabla^2\rho(\mathbf{r})$, should be in the range from 0.024 to 0.139 a.u. [50]. Additionally, there are factors indicating the existence of non-covalent interactions, and they are the following: (i) $-G(\mathbf{r})/V(\mathbf{r}) > 1$ and (ii) the positive value of $H(\mathbf{r})$. We analyzed the voids located in between the interacting **Tax**, graphene, and N-graphenes, and selected the corresponding BCPs (3,−1). The QTAIM data on BCPs for possible H-bonds between **Tax** and **G** are summarized in Table 2. The QTAIM parameters for **Tax/2N-G**, **Tax/Npyrr-G**, and **Tax/Npyrid-G** are given in Tables 3–5, respectively. We verify three, two, four and one intermolecular H-bonds in the **Tax/G**, **Tax/2N-G**, **Tax/Npyrr-G**, and **Tax/Npyrid-G** complexes, respectively. Additionally, the existence of non-covalent bonding has been proved. To sum up, according to the QTAIM analysis, all the complexes exhibit both non-covalent interactions between species and H-bonding. No indicators of covalent bonding have been found.

Table 2. Topological parameters at the BCPs (3,−1) for the **Tax/G** complex.

No.	BCPs (3,−1)	$\rho(\mathbf{r})$	$\nabla^2\rho(\mathbf{r})$	$\mathbf{G}(\mathbf{r})$	$\mathbf{V}(\mathbf{r})$	$\mathbf{H}(\mathbf{r})$	$-\mathbf{G}(\mathbf{r})/\mathbf{V}(\mathbf{r})$
1	117	0.009	0.026	0.006	−0.005	0.0008	1.2
2	159	0.009	0.029	0.006	−0.005	0.0010	1.2
3	188	0.007	0.018	0.004	−0.003	0.0008	1.3
4	216	0.010	0.032	0.007	−0.006	0.0009	1.2

Table 3. Topological parameters at the BCPs (3,−1) for the **Tax/2N-G** complex.

Species	BCPs (3,−1)	$\rho(\mathbf{r})$	$\nabla^2\rho(\mathbf{r})$	$\mathbf{G}(\mathbf{r})$	$\mathbf{V}(\mathbf{r})$	$\mathbf{H}(\mathbf{r})$	$-\mathbf{G}(\mathbf{r})/\mathbf{V}(\mathbf{r})$
1	203	0.017	0.050	0.012	−0.011	0.0008	1.09
2	246	0.006	0.017	0.004	−0.003	0.0004	1.33
3	277	0.008	0.022	0.005	−0.004	0.0007	1.25
4	287	0.015	0.036	0.008	−0.008	0.0006	1.00

Table 4. Topological parameters at the BCPs (3,−1) for the **Tax/Npyrr-G** complex.

Species	BCPs (3,−1)	$\rho(\mathbf{r})$	$\nabla^2\rho(\mathbf{r})$	$\mathbf{G}(\mathbf{r})$	$\mathbf{V}(\mathbf{r})$	$\mathbf{H}(\mathbf{r})$	$-\mathbf{G}(\mathbf{r})/\mathbf{V}(\mathbf{r})$
1	153	0.013	0.041	0.009	−0.008	0.0009	1.13
2	161	0.008	0.024	0.005	−0.004	0.0009	1.25
3	199	0.015	0.039	0.009	−0.009	0.0005	1.00
4	226	0.011	0.033	0.007	−0.006	0.0009	1.17

Table 5. Topological parameters at the BCPs (3,−1) for the **Tax/Npyrid-G** complex.

Species	BCPs (3,−1)	$\rho(\mathbf{r})$	$\nabla^2\rho(\mathbf{r})$	$\mathbf{G}(\mathbf{r})$	$\mathbf{V}(\mathbf{r})$	$\mathbf{H}(\mathbf{r})$	$-\mathbf{G}(\mathbf{r})/\mathbf{V}(\mathbf{r})$
1	138	0.007	0.018	0.004	−0.003	0.0008	1.33
2	168	0.016	0.050	0.011	−0.009	0.0015	1.22
3	236	0.005	0.013	0.003	−0.002	0.0006	1.50

The next component of interest is the induction interactions. The E_{ind} term contributes only marginally to the total attraction (~7–8%). Although absolute values of E_{ind} increase from **G** to **N-graphenes** (−4.80 (**G**), −7.46 (**Npyrid-G**), −6.21 (**Npyrr-G**), and −9.18 (**2N-G**) kcal/mol), its relative contribution remains nearly the same (we can see only small increase of 1–2%) (Table 1). It witnesses that permanent dipole moments of **N-graphenes** (3.18, 1.95, and 3.28 D for **2N-G**, **Npyrr-G**, and **Npyrid-G**, respectively) affect the strength of intermolecular interactions, and it leads to more favorable **Tax** adsorption. These effects, however, are rather small, and the E_{ind} term contributions are smaller than those of E_{el} .

We now turn to the discussions on London dispersion interactions, which contribute significantly to attraction in all cases (see Table 1 and Figure 3). For **G** and **N-graphenes**, the E_{disp} relative contributions are of roughly the same magnitude, but there is a striking difference in their absolute values. Indeed, E_{disp} increases by absolute value from −46.32 (**G**) to −68.02 (**2N-G**) kcal/mol. Moreover, its relative contribution to the attractive interactions is very large (>60%), and the order of the energy constituents is as follows: $E_{\text{disp}} > E_{\text{el}} > E_{\text{ind}}$. From the analysis of the relative inputs of energy terms to attraction, it becomes clear that the dispersion term is roughly several per cent smaller in the **2N-G** case and that this is compensated for by a simultaneous increase in the induction and electrostatic contributions.

Our previous work studied **Tax** interactions with a fragment of the arabinogalactan molecule [51]. In contrast to the present report, the E_{el} and E_{disp} terms were of almost equal importance for the stabilization. In addition, we detect numerous H-bonds between two interacting species. Another theoretical work studied adsorption of different flavonoids (quercetin, luteolin, and kaempferol) on graphene oxide [19]. It was established that the main driving force for favorable adsorption are π - π interactions and H-bonding. As a whole, our conclusions are similar to those obtained previously [19], but the SAPT0 method is not able to separate H-bonding from E_{int} . Instead of that, the substantial portion of H-bonding is included in the E_{ind} term. However, in our case, the E_{ind} terms are rather small, and, supposedly, the E_{disp} dominates.

We further compare behavior of all studied complexes at different temperatures ($T = 77$ K (liquid nitrogen temperature) and $T = 300$ K (room temperature)) by using results of ab initio molecular dynamics (AIMD) simulations. Although both classical MD [52] with empirically derived forces and AIMD with forces derived from DFT calculations can be suitable for this purpose, we select the AIMD method. It becomes popular owing to its advantages, e.g., transferability between systems and ability to accurately describe polarization and charge transfer [53]. For the **Tax/G** complex and $T = 77$ K, we observe only minor changes in the mutual configuration of the complex (Figure 4). The arrangement of **Tax** and **G** species is preserved during the whole period of simulation. Only small changes in the framework of **G** can be observed. For $T = 300$ K, the larger changes of the framework of **G** can be noticed, and the sheet of **G** acquires the corrugated shape. At the same time, the distances between **Tax** and **G** are nearly equal during the simulation time.

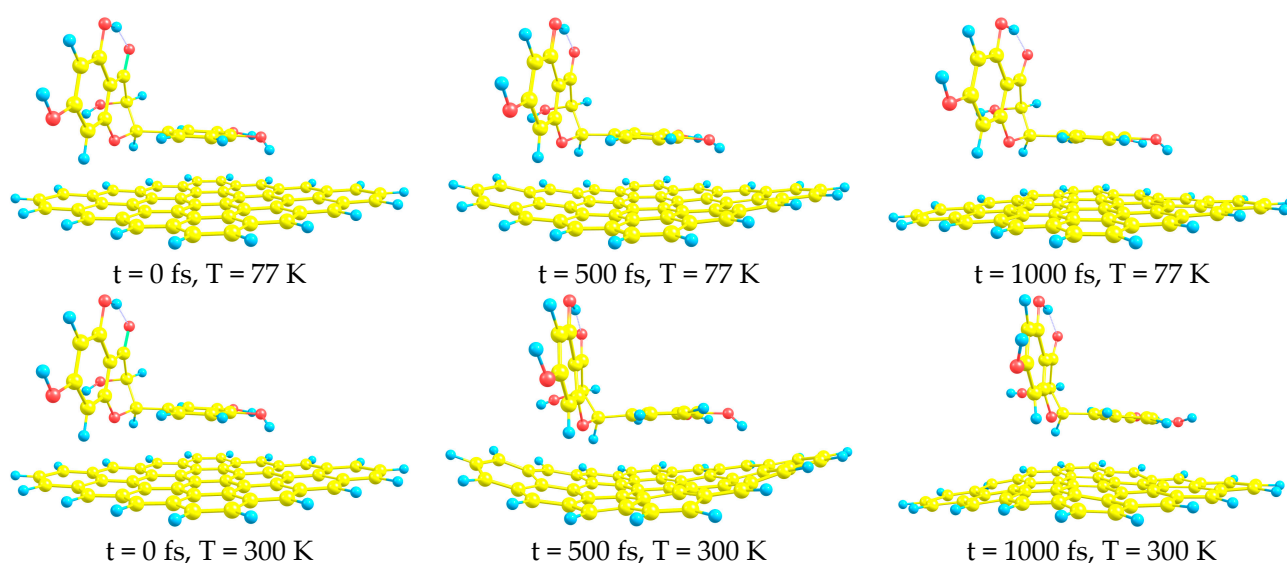


Figure 4. AIMD simulations of the **Tax/G** complex. Atomic color code: hydrogen—light blue, oxygen—red, and carbon—yellow.

A similar situation exists for the **Tax/2N-G** complex and $T = 77$ K (Figure 5). We may observe only marginal changes in both the molecular geometry and the distances between **Tax** and **2N-G**. For $T = 300$ K, the **2N-G** sheet acquires a slightly curved shape, but generally smaller changes compared to the previous case can be noticed. In all considered cases, the **Tax** molecule is in the physisorbed state throughout the simulation.

For the **Tax/Npyrr-G** complex and $T = 77$ K, we detect very small mutual reorientations of **Tax** and **Npyrr-G** species (Figure 6). For the higher $T = 300$ K, the displacement of **Tax** is slightly larger, but it generally retains its initial location. The framework of **Npyrr-G** is almost intact in these two cases. For the **Tax/Npyrid-G** complex (Figure 7), we can detect very small displacements for the lower $T = 77$ K, and slightly larger displacements/distortions for the case of $T = 300$ K. No sufficient shifts of **Tax** from the initial positions can be found for **Tax/Npyrid-G** simulations. The distances between the center-of-mass (COM) of **Tax**

and studied N-graphenes are summarized in Table S1. They are determined as the perpendicular line dropped from the COM to the underlying surface. While the simulation is proceeding, changes of the distances are taking place in studied systems. The comparison of the distances shows that the travelling of **Tax** is much smaller in the case of $T = 77$ K, and the larger distance can be observed in the case of Npyrr-G (>4 Å). As a whole, the AIMD analysis confirms the stable behavior of **Tax** adsorbed on both pristine graphene and N-doped graphenes.

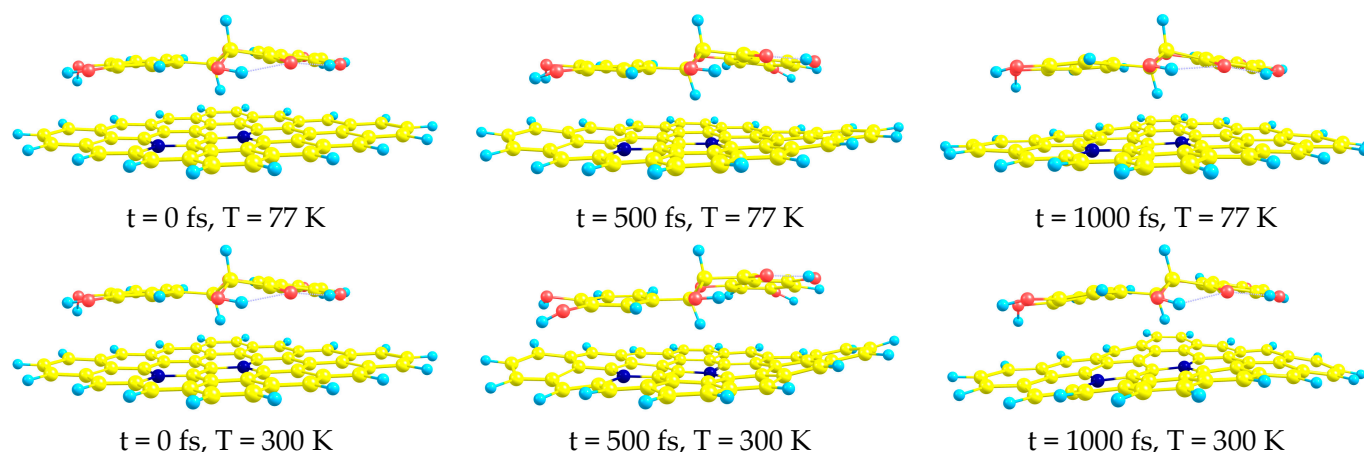


Figure 5. AIMD simulations of the **Tax/2N-G** complex. Atomic color code: hydrogen—light blue, oxygen—red, carbon—yellow, and nitrogen—blue.

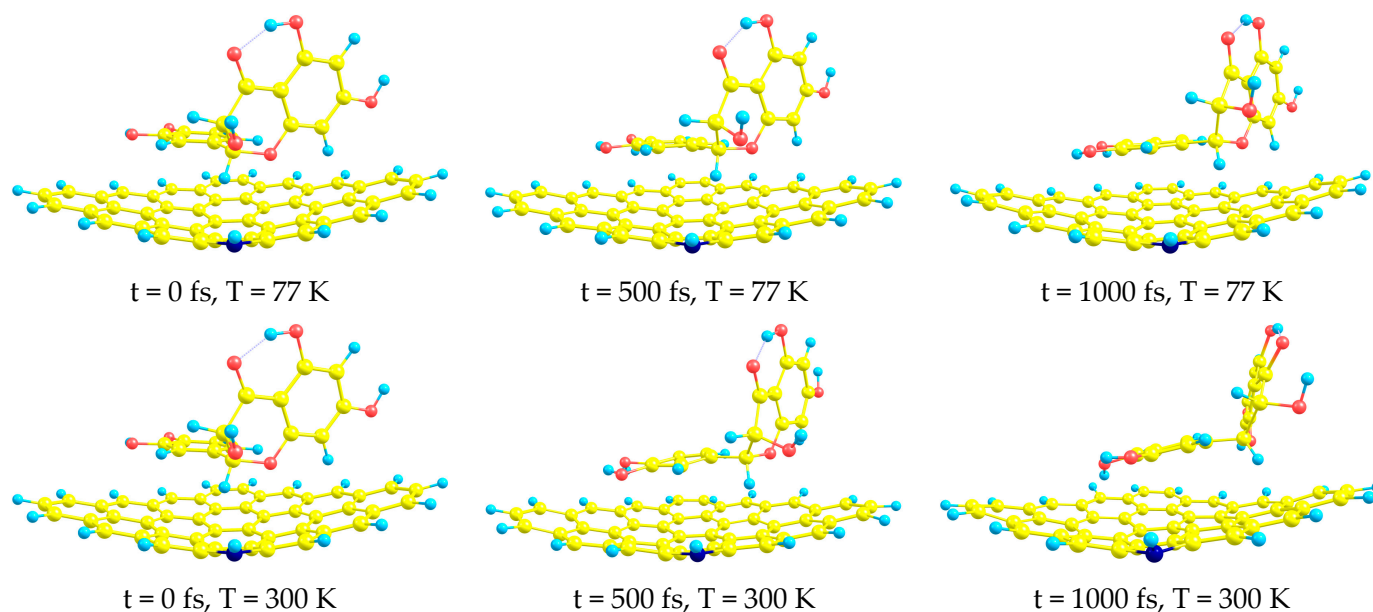


Figure 6. AIMD simulations of the **Tax/Npyrr-G** complex. Atomic color code: hydrogen—light blue, oxygen—red, carbon—yellow, and nitrogen—blue.

In addition to this, it is worth considering the solvent effects on the studied complexes as solvent environments in DDSs are important for their accurate description [54]. The first solvent used is water. We should keep in mind that **Tax** has a poor solubility in pure water, and the large graphene clusters are hydrophobic. It must also be kept in mind that the **Tax** molecules change its solubility markedly with change of temperature, and the small graphene clusters (like those involved in the present work) are water-soluble [55]. We, therefore, use water as a reference by adding explicitly six water molecules in the void between **Tax** and N-graphenes (Figure S6). A 50% ethanol–water mixture was also

employed in this work as the second solvent as this mixture allows Tax to be dissolved. To mimic this solvent, we add the 3:3 ratio of water and ethanol molecules. For the aim of comparison, gas phase calculations were also made.

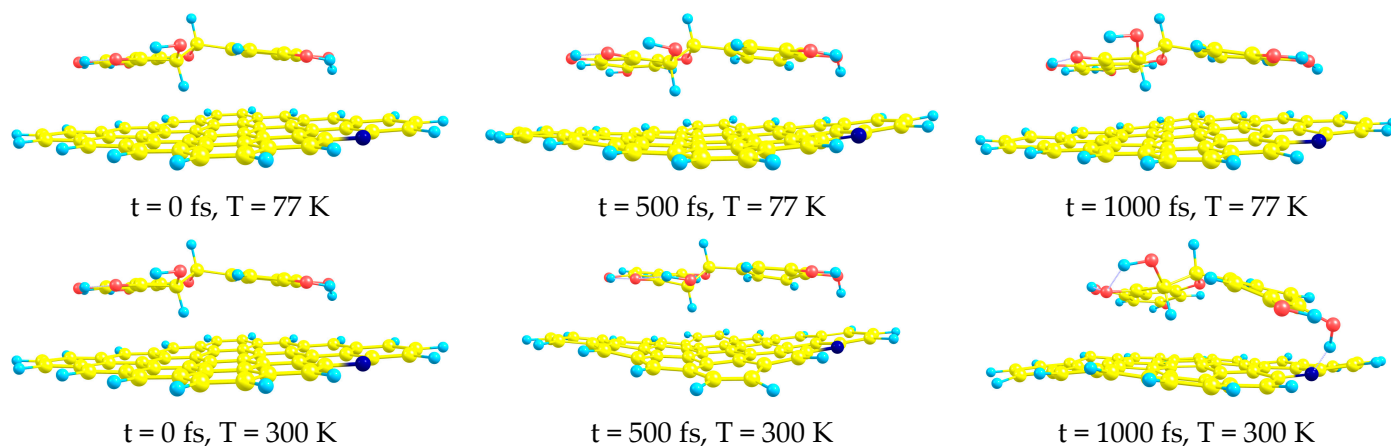


Figure 7. AIMD simulations of the **Tax/Npyrid-G** complex. Atomic color code: hydrogen—light blue, oxygen—red, carbon—yellow, and nitrogen—blue.

Now we calculate the $E_{\text{int},s}$ values based on the supermolecular approach (Table 6).

$$E_{\text{int},s} = E_{\text{comp}} - E_{\text{Tax}} - E_{\text{N-graphene}} - E_{\text{solv}}$$

where E_{comp} is the energy of the studied complex, E_{Tax} is the energy of **Tax**, $E_{\text{N-graphene}}$ is the energy of corresponding N-graphene, and E_{solv} is the energy of solvent molecules used.

Table 6. $E_{\text{int},s}$ (kcal/mol) for interactions between **Tax** and the studied adsorbents obtained via the supramolecular approach.

Adsorbent	$E_{\text{int},s}$ No Solvent	$E_{\text{int},s}$ 3:3 w:e	$E_{\text{int},s}$ 6 w
G	−33.02	−130.00	−141.58
Npyrid-G	−44.30	−146.90	−144.52
Npyrr-G	−32.63	−143.68	−139.42
2N-G	−50.65	−142.12	−145.85

When being involved, the solvents lead to a substantial stabilization of all complexes (Table 6). The $E_{\text{int},s}$ change varies from a three (**2N-G**) to an almost five times (**Npyrr-G**) increase. We link this behavior with the formation of numerous H-bonds between the studied species and solvent molecules. This indicates the applicability of studied adsorbents as **Tax** DDSs. It should be mentioned, though, that the large magnitudes of interaction energies may complicate the drug release. To avoid this possible problem, one should modify the graphene surface or select the solvent with care. Recent papers describe the endogenous and exogenous stimuli-responsive drug delivery [56,57]. The former includes pH-sensitive, redox-responsive, and ROS-responsive (reactive oxygen species) drug delivery and release. The latter deals with NIR-responsive, thermo-responsive, and electro-responsive drug delivery. Yang et al. report the strong pH dependence of loading and release of doxorubicin hydrochloride on the graphene oxide surface. They claimed that such a dependence may be caused by the stronger H-bonding interactions under basic conditions than those under acid conditions [58]. We assume that the similar technique can be suitable for **Tax**.

To summarize, based on the present results and those obtained elsewhere, we highlight the possible ways of use for N-doped graphene. Theoretical investigations of the non-

covalent interactions between the surface of graphene and related materials from the one side and different molecules from the other side can solve the problems in applying graphene materials. The main areas of interest are biological, environmental, and material science prospective applications [59]. Based on the non-covalent interactions between graphene and various molecules, we can expect the excellent nanotechnology applications in the fields of DDSs (the results of the present work), cancer treatment, energy storage, and bioimaging. Molecular adsorption can be fine-tuned by the doping with N atoms. Such a method allows obtaining enhanced E_{int} magnitudes for adsorbate molecules. Indeed, Table 1 shows enhanced E_{int} values for **Tax** adsorption on N-graphenes compared to pristine graphene. Such graphenes can act as a substitute for Li, Na, K-decorated graphenes, providing increased E_{int} values for adsorption of small molecules. At the same time, N-graphenes are easier to handle, because there is no need to manipulate with single atoms when they are involved as an adsorbent. Another important aspect is the stability and high Young's modulus of such structures [60]. This allows N-graphenes to be used in complex adsorbent systems, where high durability is required.

4. Conclusions

To conclude, in this report, we study non-covalent interactions between the **Tax** molecule, **G**, and three N-graphenes. We obtained E_{int} values and conducted SAPT0 energy decomposition analyses of four complexes. We found a more favorable binding of **Tax** on N-graphenes compared with their pristine counterpart. The detailed outcomes are as follows:

- (1) N-doping of **G** leads to the substantial increase in E_{int} for **Tax** adsorption. The highest E_{int} value is in the case of **2N-G** (-43.42 kcal/mol), and it is much larger than that for **G** (-30.04 kcal/mol).
- (2) SAPT0 calculations revealed that dispersion interactions play the main role in the stabilization of **Tax** (64–68%). Induction interactions contribute little to total attractions (7–8%), and the effects of electrostatic interactions fall between them (23–26%).
- (3) IGM graphs visually represent the dominant character of dispersion interactions. Besides this, the existence of strong interactions (H-bonding) was revealed. The QTAIM method approves the existence of H-bonding in all the studied complexes.
- (4) AIMD simulations confirm the stability of all complexes at both studied temperatures ($T = 77$ and $T = 300$ K).

The obtained results are of special importance for further experimental and theoretical research of N-doped graphenes as systems for DDSs, in particular in the field of study of natural compounds with excellent pharmacological properties.

Supplementary Materials: The following supporting information can be downloaded at: <https://www.mdpi.com/article/10.3390/solids5030023/s1>. Cartesian coordinates of studied structures, IGM description. Figure S1. Different configurations of **Tax/G** complexes. Figure S2. Different configurations of **Tax/2N-G** complexes. Figure S3. Different configurations of **Tax/Npyrr-G** complexes. Figure S4. Different configurations of **Tax/Npyrid-G** complexes. Figure S5. $C_{54}H_{18}$ (left) and $C_{80}H_{22}$ structures used as references. Figure S6. Different configurations of **Tax/N-graphenes** complexes with two solvents employed. Table S1. The distances (\AA) between center-of-mass of **Tax** and the studied adsorbents. Table S2. Cartesian coordinates of studied structures.

Funding: This work was supported by Ministry of Science and Higher Education of the Russian Federation (grant No. FZZS-2024-0002).

Institutional Review Board Statement: Not applicable.

Informed Consent Statement: Not applicable.

Data Availability Statement: Data is contained within the article or supplementary material.

Acknowledgments: The generous allotment of computational time from the Computational Center of Novosibirsk State University (www.nusc.ru) is gratefully acknowledged.

Conflicts of Interest: The authors declare no conflicts of interest.

References

1. Laffleur, F.; Keckeis, V. Advances in drug delivery systems: Work in progress still needed? *Int. J. Pharm. X* **2020**, *2*, 100050. [[CrossRef](#)] [[PubMed](#)]
2. Ezike, T.C.; Okpala, U.S.; Onoja, U.L.; Nwike, C.P.; Ezeako, E.C.; Okpara, O.J.; Okoroafor, C.C.; Eze, S.C.; Kalu, O.L.; Odoh, E.C.; et al. Advances in drug delivery systems, challenges and future directions. *Heliyon* **2023**, *9*, e17488. [[CrossRef](#)] [[PubMed](#)]
3. Zhdanov, V.P. Diffusion-Limited Release of Molecules from Nanocarriers with Appreciable Energetic Heterogeneity. *J. Phys. Chem. C* **2024**, *128*, 1216–1221. [[CrossRef](#)]
4. Peer, D.; Karp, J.M.; Hong, S.; Farokhzad, O.C.; Margalit, R.; Langer, R. Nanocarriers as an emerging platform for cancer therapy. *Nat. Nanotechnol.* **2007**, *2*, 751–760. [[CrossRef](#)] [[PubMed](#)]
5. Din, F.U.; Aman, W.; Ullah, I.; Qureshi, O.S.; Mustapha, O.; Shafique, S.; Zeb, A. Effective use of nanocarriers as drug delivery systems for the treatment of selected tumors. *Int. J. Nanomed.* **2017**, *12*, 7291–7309. [[CrossRef](#)] [[PubMed](#)]
6. Huda, S.; Alam, M.A.; Sharma, P.K. Smart nanocarriers-based drug delivery for cancer therapy: An innovative and developing strategy. *J. Drug Deliv. Sci. Technol.* **2020**, *60*, 102018. [[CrossRef](#)]
7. Liu, J.; Cui, L.; Losic, D. Graphene and graphene oxide as new nanocarriers for drug delivery applications. *Acta Biomater.* **2013**, *9*, 9243–9257. [[CrossRef](#)]
8. Oliveira, A.M.L.; Machado, M.; Silva, G.A.; Bitoque, D.B.; Tavares Ferreira, J.; Pinto, L.A.; Ferreira, Q. Graphene Oxide Thin Films with Drug Delivery Function. *Nanomaterials* **2022**, *12*, 1149. [[CrossRef](#)]
9. Khodadadei, F.; Safarian, S.; Ghanbari, N. Methotrexate-loaded nitrogen-doped graphene quantum dots nanocarriers as an efficient anticancer drug delivery system. *Mater. Sci. Engineering. C Mater. Biol. Appl.* **2017**, *79*, 280–285. [[CrossRef](#)]
10. Zare, H.; Ahmadi, S.; Ghasemi, A.; Ghanbari, M.; Rabiee, N.; Bagherzadeh, M.; Karimi, M.; Webster, T.J.; Hamblin, M.R.; Mostafavi, E. Carbon Nanotubes: Smart Drug/Gene Delivery Carriers. *Int. J. Nanomed.* **2021**, *16*, 1681–1706. [[CrossRef](#)]
11. Bartkowski, M.; Giordani, S. Carbon nano-onions as potential nanocarriers for drug delivery. *Dalton Trans.* **2021**, *50*, 2300–2309. [[CrossRef](#)]
12. Gurunathan, S.; Kim, J.H. Synthesis, toxicity, biocompatibility, and biomedical applications of graphene and graphene-related materials. *Int. J. Nanomed.* **2016**, *11*, 1927–1945. [[CrossRef](#)] [[PubMed](#)]
13. Shim, G.; Kim, M.G.; Park, J.Y.; Oh, Y.K. Graphene-based nanosheets for delivery of chemotherapeutics and biological drugs. *Adv. Drug Deliv. Rev.* **2016**, *105*, 205–227. [[CrossRef](#)] [[PubMed](#)]
14. Das, A.; Baidya, R.; Chakraborty, T.; Samanta, A.K.; Roy, S. Pharmacological basis and new insights of taxifolin: A comprehensive review. *Biomed. Pharmacother. Biomed. Pharmacother.* **2021**, *142*, 112004. [[CrossRef](#)] [[PubMed](#)]
15. Sundaraman, G.; Jayakumari, L.S. Meticulous Taxifolin Releasing Performance by the Zinc Oxide Nanoparticles: As a Short Road to Drug delivery System for Cancer Therapeutics. *J. Clust. Sci.* **2019**, *31*, 241–255. [[CrossRef](#)]
16. Luneva, O.V.; Bikova, K.; Kashurin, A.I.; Motovilov, V.V.; Uspenskaya, M.V. Thermosensitive and pH-sensitive Drug Release from Taxifolin-Containing Collagen-Acrylic Hydrogels. In Proceedings of the 2022 IEEE-EMBS Conference on Biomedical Engineering and Sciences (IECBES), Kuala Lumpur, Malaysia, 7–9 December 2022; pp. 350–354. [[CrossRef](#)]
17. Li, Y.; Su, H.; Wang, W.; Yin, Z.; Li, J.e.; Yuan, E.; Zhang, Q. Fabrication of taxifolin loaded zein-caseinate nanoparticles and its bioavailability in rat. *Food Sci. Hum. Wellness* **2023**, *12*, 2306–2313. [[CrossRef](#)]
18. Kalinina, I.; Potoroko, I.; Sonawane, S.H. Sonochemical encapsulation of taxifolin into cyclodextrine for improving its bioavailability and bioactivity for food. In *Encapsulation of Active Molecules and Their Delivery System*; Elsevier: Amsterdam, The Netherlands, 2020; pp. 85–102. [[CrossRef](#)]
19. Zhao, M.; Zhang, Y.; Qin, W.; Guo, J. First-principles study of the adsorption of flavonoids on graphene oxide. *J. Phys. Org. Chem.* **2022**, *35*, e4411. [[CrossRef](#)]
20. Tiwari, H.; Karki, N.; Pal, M.; Basak, S.; Verma, R.K.; Bal, R.; Kandpal, N.D.; Bisht, G.; Sahoo, N.G. Functionalized graphene oxide as a nanocarrier for dual drug delivery applications: The synergistic effect of quercetin and gefitinib against ovarian cancer cells. *Colloids Surfaces. B Biointerfaces* **2019**, *178*, 452–459. [[CrossRef](#)]
21. García, G.; Atilhan, M.; Aparicio, S. Flavonols on graphene: A DFT insight. *Theor. Chem. Acc.* **2015**, *134*, 57. [[CrossRef](#)]
22. Lv, Q.; Si, W.; He, J.; Sun, L.; Zhang, C.; Wang, N.; Yang, Z.; Li, X.; Wang, X.; Deng, W.; et al. Selectively nitrogen-doped carbon materials as superior metal-free catalysts for oxygen reduction. *Nat. Commun.* **2018**, *9*, 3376. [[CrossRef](#)]
23. Ganyecz, A.; Kallay, M. Oxygen Reduction Reaction on N-Doped Graphene: Effect of Positions and Scaling Relations of Adsorption Energies. *J. Phys. Chemistry. C Nanomater. Interfaces* **2021**, *125*, 8551–8561. [[CrossRef](#)] [[PubMed](#)]
24. Dinadayalane, T.; Lazare, J.; Alzaaqi, N.F.; Herath, D.; Hill, B.; Campbell, A.E. Structures, properties, and applications of nitrogen-doped graphene. In *Theoretical and Computational Chemistry*; Elsevier: Amsterdam, The Netherlands, 2022; Volume 21, pp. 211–248. [[CrossRef](#)]
25. Olteanu, D.; Filip, A.; Socaci, C.; Biris, A.R.; Filip, X.; Coros, M.; Rosu, M.C.; Pogacean, F.; Alb, C.; Baldea, I.; et al. Cytotoxicity assessment of graphene-based nanomaterials on human dental follicle stem cells. *Colloids Surfaces. B Biointerfaces* **2015**, *136*, 791–798. [[CrossRef](#)]

26. Yokwana, K.; Ntsendwana, B.; Nxumalo, E.N.; Mhlanga, S.D. Recent advances in nitrogen-doped graphene oxide nanomaterials: Synthesis and applications in energy storage, sensor electrochemical applications and water treatment. *J. Mater. Res.* **2023**, *38*, 3239–3263. [CrossRef]
27. Jeziorski, B.; Moszynski, R.; Szalewicz, K. Perturbation Theory Approach to Intermolecular Potential Energy Surfaces of van der Waals Complexes. *Chem. Rev.* **1994**, *94*, 1887–1930. [CrossRef]
28. Patkowski, K. Recent developments in symmetry-adapted perturbation theory. *WIREs Comput. Mol. Sci.* **2019**, *10*, e1452. [CrossRef]
29. Bader, R.F.W. A quantum theory of molecular structure and its applications. *Chem. Rev.* **1991**, *91*, 893–928. [CrossRef]
30. Lefebvre, C.; Rubez, G.; Khartabil, H.; Boisson, J.-C.; Contreras-García, J.; Hénon, E. Accurately extracting the signature of intermolecular interactions present in the NCI plot of the reduced density gradient versus electron density. *Phys. Chem. Chem. Phys.* **2017**, *19*, 17928–17936. [CrossRef] [PubMed]
31. Lefebvre, C.; Khartabil, H.; Boisson, J.-C.; Contreras-García, J.; Piquemal, J.-P.; Hénon, E. The Independent Gradient Model: A New Approach for Probing Strong and Weak Interactions in Molecules from Wave Function Calculations. *ChemPhysChem* **2018**, *19*, 724–735. [CrossRef] [PubMed]
32. Lee, C.; Yang, W.; Parr, R.G. Development of the Colle-Salvetti correlation-energy formula into a functional of the electron density. *Phys. Rev. B* **1988**, *37*, 785–789. [CrossRef]
33. Becke, A.D.; Edgecombe, K.E. A simple measure of electron localization in atomic and molecular systems. *J. Chem. Phys.* **1990**, *92*, 5397–5403. [CrossRef]
34. Weigend, F.; Ahlrichs, R. Balanced basis sets of split valence, triple zeta valence and quadruple zeta valence quality for H to Rn: Design and assessment of accuracy. *Phys. Chem. Chem. Phys.* **2005**, *7*, 3297. [CrossRef]
35. Neese, F.; Wennmohs, F.; Becker, U.; Riplinger, C. The ORCA quantum chemistry program package. *J. Chem. Phys.* **2020**, *152*, 224108. [CrossRef]
36. Grimme, S.; Antony, J.; Ehrlich, S.; Krieg, H. A consistent and accurate ab initio parametrization of density functional dispersion correction (DFT-D) for the 94 elements H-Pu. *J. Chem. Phys.* **2010**, *132*, 154104. [CrossRef]
37. Qu, Z.; Sun, F.; Liu, X.; Gao, J.; Qie, Z.; Zhao, G. The effect of nitrogen-containing functional groups on SO₂ adsorption on carbon surface: Enhanced physical adsorption interactions. *Surf. Sci.* **2018**, *677*, 78–82. [CrossRef]
38. Petrushenko, I.K.; Tikhonov, N.I.; Petrushenko, K.B. Graphene-BN-organic nanoflake complexes: DFT, IGM and SAPT0 insights. *Diam. Relat. Mater.* **2020**, *107*, 107905. [CrossRef]
39. Hohenstein, E.G.; Sherrill, C.D. Wavefunction methods for noncovalent interactions. *Wiley Interdiscip. Rev. Comput. Mol. Sci.* **2012**, *2*, 304–326. [CrossRef]
40. Hohenstein, E.G.; Sherrill, C.D. Density fitting and Cholesky decomposition approximations in symmetry-adapted perturbation theory: Implementation and application to probe the nature of π - π interactions in linear acenes. *J. Chem. Phys.* **2010**, *132*, 184111. [CrossRef]
41. Turney, J.M.; Simmonett, A.C.; Parrish, R.M.; Hohenstein, E.G.; Evangelista, F.A.; Fermann, J.T.; Mintz, B.J.; Burns, L.A.; Wilke, J.J.; Abrams, M.L.; et al. Psi4: An open-source ab initio electronic structure program. *Wiley Interdiscip. Rev. Comput. Mol. Sci.* **2012**, *2*, 556–565. [CrossRef]
42. de la Roza, A.O.; DiLabio, G.A. *Non-Covalent Interactions in Quantum Chemistry and Physics: Theory and Applications*; Elsevier: Amsterdam, The Netherlands, 2017; p. 476.
43. Wang, Y.; Shao, Y.; Matson, D.W.; Li, J.; Lin, Y. Nitrogen-doped graphene and its application in electrochemical biosensing. *ACS Nano* **2010**, *4*, 1790–1798. [CrossRef]
44. Petrushenko, I.K.; Petrushenko, K.B. Hydrogen physisorption on nitrogen-doped graphene and graphene-like boron nitride-carbon heterostructures: A DFT study. *Surf. Interfaces* **2019**, *17*, 100355. [CrossRef]
45. Petrushenko, I.K.; Petrushenko, K.B. Adsorption of diatomic molecules on nitrogenated holey graphene: Theoretical insights. *Surf. Interfaces* **2021**, *27*, 101446. [CrossRef]
46. Lu, T.; Chen, F. Multiwfn: A multifunctional wavefunction analyzer. *J. Comput. Chem.* **2012**, *33*, 580–592. [CrossRef] [PubMed]
47. Humphrey, W.; Dalke, A.; Schulten, K. VMD: Visual molecular dynamics. *J. Mol. Graph.* **1996**, *14*, 33–38. [CrossRef]
48. Chemcraft—Graphical Software for Visualization of Quantum Chemistry Computations. Available online: <http://www.chemcraftprog.com> (accessed on 1 February 2024).
49. Pykal, M.; Jurecka, P.; Karlicky, F.; Otyepka, M. Modelling of graphene functionalization. *Phys. Chem. Chem. Phys.* **2016**, *18*, 6351–6372. [CrossRef] [PubMed]
50. Koch, U.; Popelier, P.L.A. Characterization of C-H-O Hydrogen Bonds on the Basis of the Charge Density. *J. Phys. Chem.* **1995**, *99*, 9747–9754. [CrossRef]
51. Petrushenko, I.K.; Ivanov, N.A. Non-covalent interactions between dihydroquercetin and arabinogalactan molecules: Theoretical study. *Comput. Theor. Chem.* **2023**, *1230*, 114394. [CrossRef]
52. Gotzias, A.; Tocci, E.; Sapalidis, A. Solvent-Assisted Graphene Exfoliation from Graphite Using Umbrella Sampling Simulations. *Langmuir* **2023**, *39*, 18437–18446. [CrossRef] [PubMed]
53. Crabb, E.; France-Lanord, A.; Leverick, G.; Stephens, R.; Shao-Horn, Y.; Grossman, J.C. Importance of Equilibration Method and Sampling for Ab Initio Molecular Dynamics Simulations of Solvent-Lithium-Salt Systems in Lithium-Oxygen Batteries. *J. Chem. Theory Comput.* **2020**, *16*, 7255–7266. [CrossRef]

54. Manna, K.; Huang, H.-N.; Li, W.-T.; Ho, Y.-H.; Chiang, W.-H. Toward Understanding the Efficient Exfoliation of Layered Materials by Water-Assisted Cosolvent Liquid-Phase Exfoliation. *Chem. Mater.* **2016**, *28*, 7586–7593. [[CrossRef](#)]
55. Lin, H.A.; Sato, Y.; Segawa, Y.; Nishihara, T.; Sugimoto, N.; Scott, L.T.; Higashiyama, T.; Itami, K. A Water-Soluble Warped Nanographene: Synthesis and Applications for Photoinduced Cell Death. *Angew. Chem.* **2018**, *57*, 2874–2878. [[CrossRef](#)]
56. Khakpour, E.; Salehi, S.; Naghib, S.M.; Ghorbanzadeh, S.; Zhang, W. Graphene-based nanomaterials for stimuli-sensitive controlled delivery of therapeutic molecules. *Front. Bioeng. Biotechnol.* **2023**, *11*, 1129768. [[CrossRef](#)] [[PubMed](#)]
57. Hoseini-Ghahfarokhi, M.; Mirkiani, S.; Mozaffari, N.; Abdolahi Sadatlu, M.A.; Ghasemi, A.; Abbaspour, S.; Akbarian, M.; Farjadian, F.; Karimi, M. Applications of Graphene and Graphene Oxide in Smart Drug/Gene Delivery: Is the World Still Flat? *Int. J. Nanomed.* **2020**, *15*, 9469–9496. [[CrossRef](#)] [[PubMed](#)]
58. Yang, X.; Zhang, X.; Liu, Z.; Ma, Y.; Huang, Y.; Chen, Y. High-Efficiency Loading and Controlled Release of Doxorubicin Hydrochloride on Graphene Oxide. *J. Phys. Chem. C* **2008**, *112*, 17554–17558. [[CrossRef](#)]
59. Zhan, J.; Lei, Z.; Zhang, Y. Non-covalent interactions of graphene surface: Mechanisms and applications. *Chem* **2022**, *8*, 947–979. [[CrossRef](#)]
60. Mehrabani, M.; Khatibi, M.M.; Ashory, M.R.; Sadeghzadeh, S. Effect of nitrogen or boron impurities on the mechanical and vibrational properties of graphene nanosheets: A molecular dynamics approach. *Micro Nano Lett.* **2020**, *15*, 977–983. [[CrossRef](#)]

Disclaimer/Publisher’s Note: The statements, opinions and data contained in all publications are solely those of the individual author(s) and contributor(s) and not of MDPI and/or the editor(s). MDPI and/or the editor(s) disclaim responsibility for any injury to people or property resulting from any ideas, methods, instructions or products referred to in the content.